Volume 49
Number 30
14 August 2020
Pages 10281-10664

Dalton Transactions

An international journal of inorganic chemistry

rsc.li/dalton

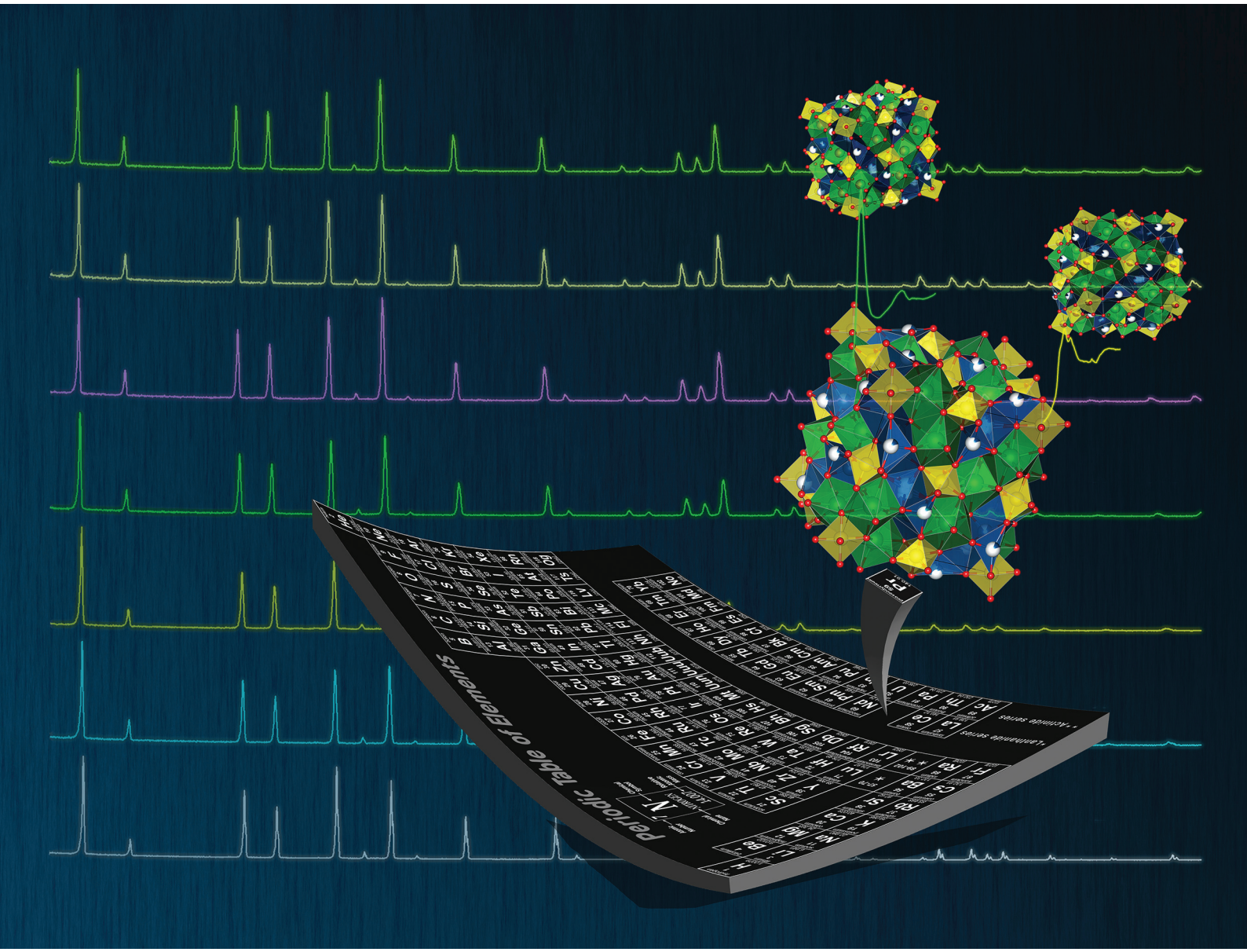

ISSN 1477-9226

ROYAL SOCIETY OF CHEMISTRY

PAPER

M. P. Stockham, P. R. Slater *et al.*
Evaluation of the effect of site substitution of Pr doping in the lithium garnet system $Li_5La_3Nb_2O_{12}$

Dalton Transactions

ROYAL SOCIETY OF CHEMISTRY

PAPER

View Article Online
View Journal | View Issue

Check for updates

Cite this: *Dalton Trans.*, 2020, **49**, 10349

Evaluation of the effect of site substitution of Pr doping in the lithium garnet system $Li_5La_3Nb_2O_{12}$†

M. P. Stockham, *[a] B. Dong,[a] Y. Ding,[b] Y. Li[b] and P. R. Slater *[a]

Li ion conducting garnets have been attracting considerable interest for use as the electrolyte in all solid-state batteries, due to their high ionic conductivity and wide electrochemical stability window. Consequently, there have been a number of doping studies aimed at optimising the conductivity, focusing on both doping in $Li_7La_3Zr_2O_{12}$ and $Li_5La_3(Nb/Ta)_2O_{12}$ systems. In this paper, we report a detailed study of Pr doping in $Li_5La_3Nb_2O_{12}$, and show that this is a rare example of an ambi-site dopant, being able to be doped onto either the La or Nb site. Interestingly the resultant Pr oxidation state is determined by the site substitution, with oxidation states of 3+ for the La site, and 4+ for the Nb site. While the conductivity is essentially unchanged for the La site substitution, Pr^{4+} substitution on the Nb site leads to a large increase in the conductivity associated with the increase in Li content ($Li_{5+x}La_3Nb_{2-x}Pr_xO_{12}$) up to 0.56 mS cm^{-1} (at 50 °C) for x = 0.8. Overall, this work highlights the flexibility of these garnet materials to doping, and suggests that further consideration of site substitution be considered for other dopants.

Received 23rd April 2020,
Accepted 29th May 2020

DOI: 10.1039/d0dt01497d

rsc.li/dalton

Open Access Article. Published on 29 May 2020. Downloaded on 8/1/2025 2:51:58 AM.
This article is licensed under a Creative Commons Attribution-NonCommercial 3.0 Unported Licence.

Introduction

Increased demand for portable electronic devices, electric vehicles and renewable energy has significantly expanded demand for efficient, safe, low cost and high-power energy storage. Lithium ion batteries (LIB) are principally used for these purposes, due to their high volumetric and gravimetric energy densities.[1] However, current LIBs have a variety of safety, thermal and efficiency issues, which are often attributed to the liquid organic electrolytes used in the cell. These liquid electrolytes also limit the cell potential by preventing the use of lithium metal anodes.[2] These disadvantages, and advantages, are covered in many review articles.[1,3–7] Therefore, the replacement of liquid electrolytes with a solid-state electrolyte (SSE) to give an all solid-state battery (ASSB) remains the key challenge to deliver this next leap in energy storage.[8] Such batteries, when compared to traditional LIBs, offer the potential for increased safety, operate over a wider electrochemical window, have increased thermal stability and are ideally stable against Li metal, hence increasing energy density per cell.[8–12]

As a result, there is considerable interest in the identification and optimisation of new solid state electrolyte materials. However, many of these electrolytes, such as LISICON, sulphides/glass and LiPON, are limited by either low ionic conductivity or a poor electrochemical stability window.[13–15] Of these reports, the lithium containing garnet type systems are one of the few which present with high lithium ion conductivity (reportedly >10^{-4} S cm^{-1} [16]), a wide electrochemical stability window and are chemically stable against Li metal.[9,13,17–19] Hence these systems are attracting considerable interest for use in ASSBs.

However, there still remain challenges for these garnet systems, and so there continues to be interest in new doping studies in these materials. In particular, there is a need to further improve the ionic conductivity, as well as improve the interface between the electrolyte and electrodes.[9,10,13] Traditional garnet materials have the general formula $A_3B_2X_3O_{12}$,[13,20–22] where the A, B, C cations are located in 8, 6, 4 coordinate sites respectively. In the Li containing garnets, excess Li can be accommodated in interstitial sites, such that the general formula of these can be classed as $A_3B_2Li_{3+x}O_{12}$ ($0 \leq x \leq 4$), so that the Li content can be varied between 3 (as in $Li_3Ln_3Te_2O_{12}$), and 7 (as in $Li_7La_3(Zr/Sn/Hf)_2O_{12}$). Those systems with <7 lithium atoms crystallise in a cubic structure which has high Li-ion conductivity. In contrast, the stoichiometric $Li_7La_3(Zr/Sn/Hf)_2O_{12}$ systems crystallise in the less conductive tetragonal phase, although doping to reduce the Li content allows the formation of the cubic cell with enhanced conductivity.

For cubic garnets, such as $Li_5La_3Nb_2O_{12}$ (LLNO), ionic migration pathways have been attributed to two tetrahedral sites bridged by a single face sharing octahedron. As the lithium sites are not fully occupied in these systems, lithium

[a]School of Chemistry, University of Birmingham, Birmingham B15 2TT, UK. E-mail: p.r.slater@bham.ac.uk
[b]School of Chemical Engineering, University of Birmingham, Birmingham B15 2TT, UK

†Electronic supplementary information (ESI) available. See DOI: 10.1039/d0dt01497d

Open Access Article. Published on 29 May 2020. Downloaded on 8/1/2025 2:51:58 AM.
This article is licensed under a Creative Commons Attribution-NonCommercial 3.0 Unported Licence.

partially occupies the interstitial octahedral sites 48 h and 96 g, in a disordered fashion. This gives a disordered Li sublattice and a migration pathway which leads to high ionic conductivity *via* the Li^+ charge carrier, which is thought to follow the hopping mechanism of 24 d → 96 h → 48 g → 96 h → 24 d, as determined by high temperature neutron diffraction studies.[23]

Of the wide variety of garnet systems, particular attention has been afforded to $Li_7La_3Zr_2O_{12}$ (LLZO). This stoichiometric system is tetragonal at room temperature, with comparatively low conductivity, and changes to a cubic cell at around 750° C; this temperature can be reduced to 350 °C by doping at the Zr site with Ce, leading to an increase in conductivity.[24] Stabilisation of the cubic cell at room temperature (c-LLZO) requires a reduction of the lithium content, often using Al or Ga substitution at the Li site.[16,25,26] Dopants at the Zr site (*e.g.* Nb, Ta[27,28]) also can stabilise c-LLZO.

Although c-LLZO has been reported with conductivities $>10^{-4}$ S cm^{-1}, these often require complex methodologies and/or equipment, such as field assisted sintering, which presents a barrier to commercial scalability.[16,29,30] Consequently, the majority of c-LLZO doping strategies lead to conductivities $\sim10^{-4}$ S cm^{-1}, or lower, and are suboptimal compared with current LIB liquid electrolytes.[31–38] Therefore, it is of interest to investigate alternative doping strategies of other lithium garnet systems, such as $Li_5La_3Nb_2O_{12}$ (LLNO). This system was the first to show fast Li-ion conductivity, and outside of detailed examinations of the lithium migration pathways, has now been superseded by research on c-LLZO.[39,40] However, of the prior reports of doping into the LLNO system, many show room temperature conductivities of $\sim10^{-4}$ S cm^{-1} and are thus similar to c-LLZO.[13,41] Therefore, further doping studies on the LLNO system are warranted. Herein we report an examination of Pr doping in this system. Pr was chosen because of its ability to adopt different oxidation states (3+, 4+), and so potential, based on size considerations, to dope onto either the Nb or the La site according to the following formula $Li_{5+x}La_3Nb_{2-x}Pr_xO_{12}$ (Pr^{4+}) and $Li_5La_{3-x}Pr_xNb_2O_{12}$ (Pr^{3+}). We confirm this ambi-site substitutional ability of Pr, and illustrate in particular that Pr doping on the Nb site leads to samples with high Li ion conductivity.

Methods

Synthesis

$Li_{5+x}La_3Nb_{2-x}Pr_xO_{12}$ garnets were prepared *via* the solid-state route from stochiometric quantities of Li_2CO_3, La_2O_3, Nb_2O_5 and Pr_6O_{11} under air. A 40% mol excess of lithium was added to compensate for lithium loss during high temperature sintering. All powders were ball milled for 1 h (500 rpm) and heated to 950 °C (16 hours). Impure phases ($x > 0.25$) were subsequently ball milled with a 20% lithium mol excess and heated to 950 °C (12 hours). Samples where $x \geq 0.8$ were synthesised in a dry room with a dewpoint between −45 °C to −64 °C (the elimination of humidity was found to be necessary to prepare good quality samples for these high Pr contents: it is known that moisture can be an issue in the synthesis of Li garnet systems).[42–44]

$Li_5La_{3-x}Pr_xNb_2O_{12}$ was also prepared *via* the solid-state route in either air or 5%H_2/N_2. Samples were heated to 950 °C for 16 hours, cooled to room temperature and reheated to 950 °C for 16 hours. After synthesis, all samples were stored in an argon glove box.

Characterisation

Samples were characterised by X-ray diffraction (XRD) using a Bruker D8 diffractometer with Cu Kα radiation. Cell parameters were determined from Rietveld refinement using GSAS II software.[45] In order to evaluate the Pr oxidation states X-ray absorption near edge spectroscopy (XANES) data were recorded at Diamond Light Source on beamline B18 and data interpreted *via* the Athena/Artemis software.[46] Scanning electron microscopy (SEM) was performed using a TM4000plus SEM, with elemental compositions evaluated by the corresponding AZtecOne EDX attachment. The Pr–LLNO garnet powders were placed on carbon tape, attached to the SEM stub and evaluated at 15 kV in back scattered electron mode.

Impedance spectroscopy

Pellets for conductivity measurements were prepared as follows: 10 mm diameter pellets were uniaxially hot pressed with an atlas heating platen to *ca.* 3 tonnes at 300 °C and, subsequently, heated to 1000–1050 °C for 12 hours under dry N_2 to densify the SSE membrane. During N_2 treatment sacrificial powders were used to protect pellets from Li loss and to prevent Al contamination from the Al_2O_3 crucible. Pellets were then polished, painted with gold electrodes and heated to 800 °C for 1 hour in air to cure the Au paste. The pellets were then quenched from 700 °C to limit any H^+/Li^+ on cooling, as has been shown to occur for garnet samples at lower temperatures in air.[26,47] A.C. impedance spectroscopy data were collected during heating over a temperature range of 50 °C to 250 °C (with 16 measurements taken), using a Hewlett Packard 4192A instrument. Data for the most conductive phases ($\sim10^{-4}$ S cm^{-1}) were also measured at room temperature. All measurements were conducted in air.

Results and discussion

Praseodymium doping on the Nb Site: $Li_{5+x}La_3Nb_{2-x}Pr_xO_{12}$

The powder XRD patterns for $Li_{5+x}La_3Nb_{2-x}Pr_xO_{12}$ ($0 \leq x \geq 1$) are shown in Fig. 1, illustrating pure garnet samples across the range. All patterns could be indexed based on a cubic garnet with space group $Ia\bar{3}d$ (no. 230).[22,39,40] Phases where $x > 0.25$ initially demonstrated Pr_2O_3 and La_2O_3 impurity phases which were overcome by addition of 20% excess lithium and reheating. Phases where $x > 0.8$ showed decreased conductivity (see later), hence the synthesis method was not undertaken past $x = 1$. The colour of the samples became increasingly yellow as a function of Pr content, which is attributed to the presence of

 This journal is © The Royal Society of Chemistry 2020

Open Access Article. Published on 29 May 2020. Downloaded on 8/1/2025 2:51:58 AM.
This article is licensed under a Creative Commons Attribution-NonCommercial 3.0 Unported Licence.

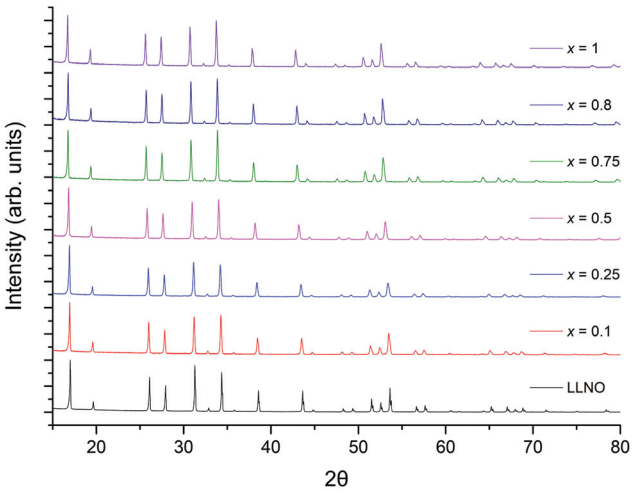

Fig. 1 Powder XRD patterns for $Li_{5+x}La_3Nb_{2-x}Pr_xO_{12}$ ($0 \leq x \geq 1$) synthesised in air, showing the formation of single phase garnet samples across the range.

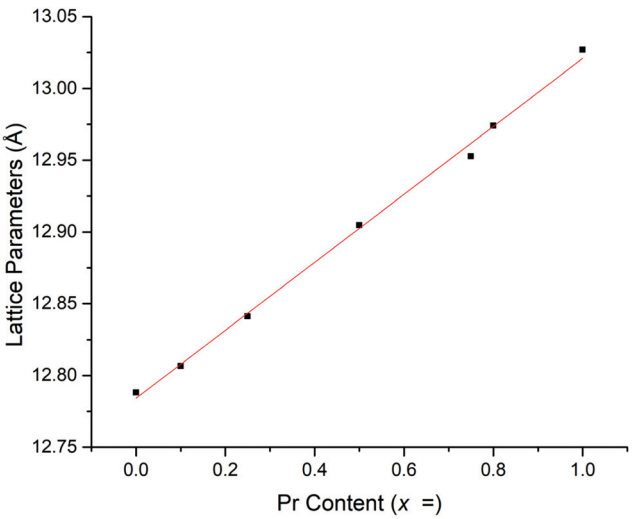

Fig. 2 Cell parameters *vs.* Pr content for $Li_{5+x}La_3Nb_{2-x}Pr_xO_{12}$.

Pr^{4+}, which is commonly believed to be responsible for the colour in the yellow pigment Pr–$ZrSiO_4$ (although some debate persists behind the chemistry of Pr–$ZrSiO_4$).[48–50]

Rietveld refinements, based on the structural model from Cussen[39] showed a linear increase in lattice parameters with increasing Pr content (Fig. 2 and Table 1), in agreement with Vegard's law and so confirming the solid solution range. This increase is due to the larger ionic radius of Pr^{4+} compared to Nb^{5+}.[39,41,51] The refined Pr occupancies on the Nb site were similar to the expected stoichiometric ratio across the series, however, did deviate slightly from the ideal ratio as the Pr content increased, see Table 1.

In order to try to confirm the Pr oxidation state, X-ray absorption near edge spectroscopy (XANES) data were collected for the $Li_{5+x}La_3Nb_{2-x}Pr_xO_{12}$ systems. However, the La L2 edge of La (~5897 eV) interfered with the Pr L3 edge (~5968 eV) to some degree. Nevertheless, when compared to the Pr^{3+} and Pr^{4+} reference (Pr_2O_3 and $BaPrO_3$ respectively), the peaks are qualitatively characteristic of Pr^{4+}, see Fig. 3. These data show a peak at 5973 eV with a shoulder at 5980 eV, which closely matches the Pr^{4+} ($BaPrO_3$) reference (Fig. 3) and can be assigned to Pr^{4+}. Further support for the assignment of Pr^{4+} in the $Li_{5.5}La_3Nb_{1.5}Pr_{0.5}O_{12}$ samples is provided by comparison with $Pr_{0.5}Ce_{0.5}O_2$, a Pr^{4+} reference used elsewhere,[52,53] which shows peaks at 5970 and 5980 eV.

Therefore, considering the XRD, XANES and refinement data, there is compelling evidence that Pr^{4+} has been doped into the LLNO structure at the Nb site (16a).

SEM and EDX

SEM and EDX on a singular grain of $Li_{5.5}La_3Nb_{1.5}Pr_{0.5}O_{12}$ demonstrated uniform Pr presence (in the expected stoichiometric ratio) when compared to La, Nb and O. However, for Pr (x) contents ≥0.5 Al contamination from the Al_2O_3 crucible became increasingly apparent[25] (Fig. 4).

Praseodymium doping on the La site (Pr^{3+}): $Li_5La_{3-x}Pr_xNb_2O_{12}$

The successful synthesis of $Li_5La_{3-x}Pr_xNb_2O_{12}$ garnets in air was limited to samples in the range $0 \leq x \leq 1$. In contrast synthesis under 5%H_2/N_2 permitted a complete solid solution range for the replacement of La with Pr, $0 \leq x \leq 3$. Both XRD patterns for air prepared samples ($0 \leq x \leq 1$) and 5%H_2 prepared samples ($0 \leq x \leq 3$) could be indexed on a cubic garnet cell with space group $Ia\bar{3}d$ (no. 230);[22,39,40] see Fig. 5 and 8 respectively. In some cases, particularly for the air-based synthesis, a small amount of Li_3NbO_4 impurity was observed marked in the respective figures (also see ESI†).

Table 1 Pellet and conductivity data in addition to lattice parameters for $Li_{5+x}La_3Nb_{2-x}Pr_xO_{12}$ samples which were uniaxially hot pressed. The Arrhenius plot $x = 1$ was not linear, hence no activation energy available

Hot pressed samples	Pellet density (g cm^{-1})	Refined density (g cm^{-1})	Relative density (%)	Lattice parameters (Å)	Pr fractional site occupancies on the Nb site	Conductivity (50 °C) (S cm^{-1})	Activation energy (eV)
LLNO reference[39]	—	5.259	—	12.79432		~ $\times 10^{-6}$	
LLNO	4.52	5.248	86	12.7880(3)		4.3×10^{-6}	0.32
$x = 0.1$	4.32	5.284	82	12.8066(3)	0.0649	5.6×10^{-5}	0.28
$x = 0.25$	4.50	5.300	85	12.8410(4)	0.1265	7.3×10^{-5}	0.32
$x = 0.5$	4.33	5.321	81	12.9048(3)	0.2568	1.6×10^{-4}	0.29
$x = 0.75$	4.72	5.361	88	12.9527(3)	0.3876	3.4×10^{-4}	0.37
$x = 0.8$	4.53	5.358	85	12.9741(5)	0.4179	5.6×10^{-4}	0.36
$x = 1$	3.50	5.366	65	13.0269(4)	0.5160	1.9×10^{-4}	—

Open Access Article. Published on 29 May 2020. Downloaded on 8/1/2025 2:51:58 AM.
This article is licensed under a Creative Commons Attribution-NonCommercial 3.0 Unported Licence.

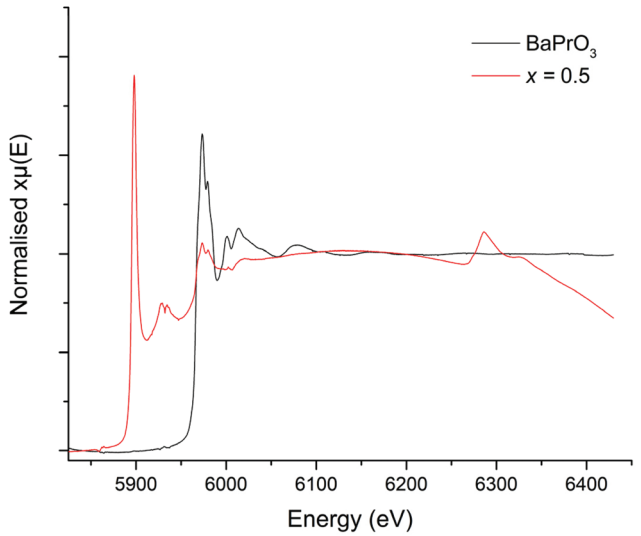

Fig. 3 XANES spectrum for $Li_{5.5}La_3Nb_{1.5}Pr_{0.5}O_{12}$ compared to $BaPrO_3$ (Pr^{4+}) reference.

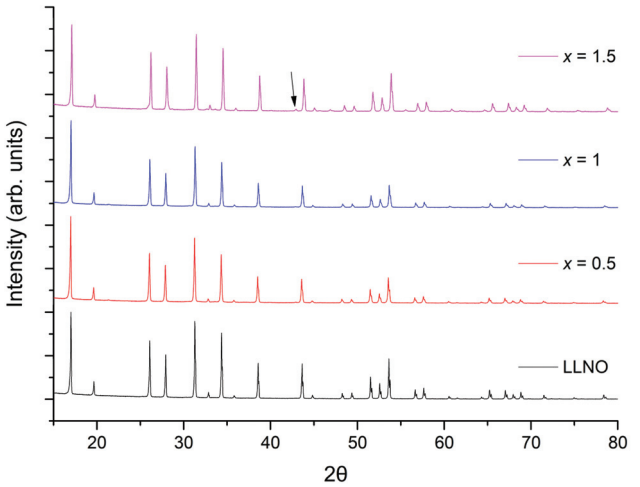

Fig. 5 The powder XRD patterns for $Li_5La_{3-x}Pr_xNb_2O_{12}$ ($0 \leq x \leq 1.5$) synthesised in air. Phase pure samples are shown up to $x = 1$, but all show garnet type symmetry. Li_3NbO_4 impurity marked by arrow. See ESI† for expanded XRD pattern.

$Li_5La_{3-x}Pr_xNb_2O_{12}$ samples prepared in air demonstrated an increasingly straw yellow/brown colour, which was distinctly different from the colour of the $Li_{5+x}La_3Nb_{2-x}Pr_xO_{12}$ samples discussed earlier. Cell parameters determined from Rietveld refinement indicated the expected decrease with increasing Pr content (due to the smaller size of Pr^{3+} *versus* La^{3+}) (Fig. 6) and

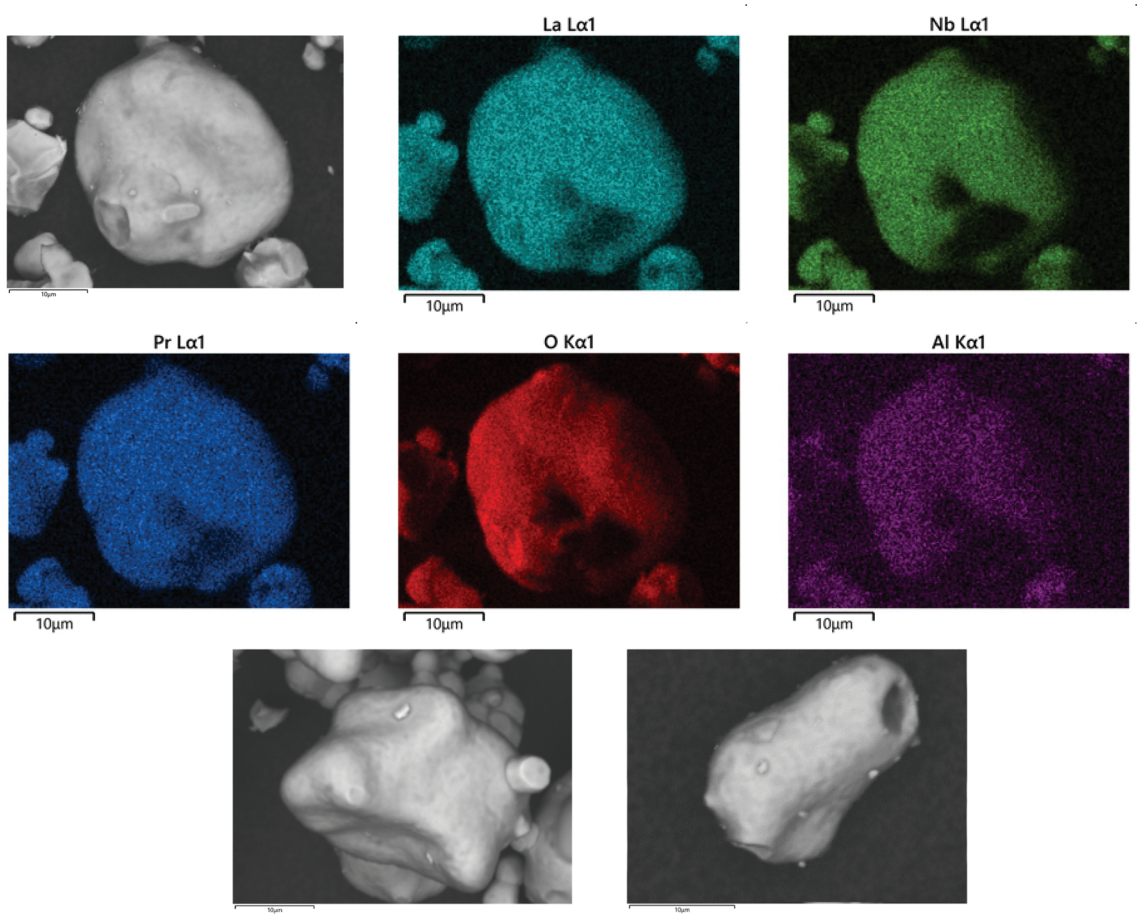

Fig. 4 SEM image and EDX map of elemental distribution in $Li_{5.5}La_3Nb_{1.5}Pr_{0.5}O_{12}$. Scale bar at 10 μm in all images.

This journal is © The Royal Society of Chemistry 2020

Open Access Article. Published on 29 May 2020. Downloaded on 8/1/2025 2:51:58 AM.
This article is licensed under a Creative Commons Attribution-NonCommercial 3.0 Unported Licence.

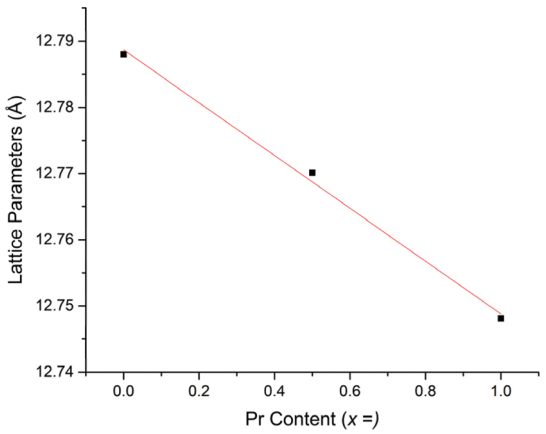

Fig. 6 Cell parameters *vs.* Pr content for air-based synthesis of $Li_5La_{3-x}Pr_xNb_2O_{12}$.

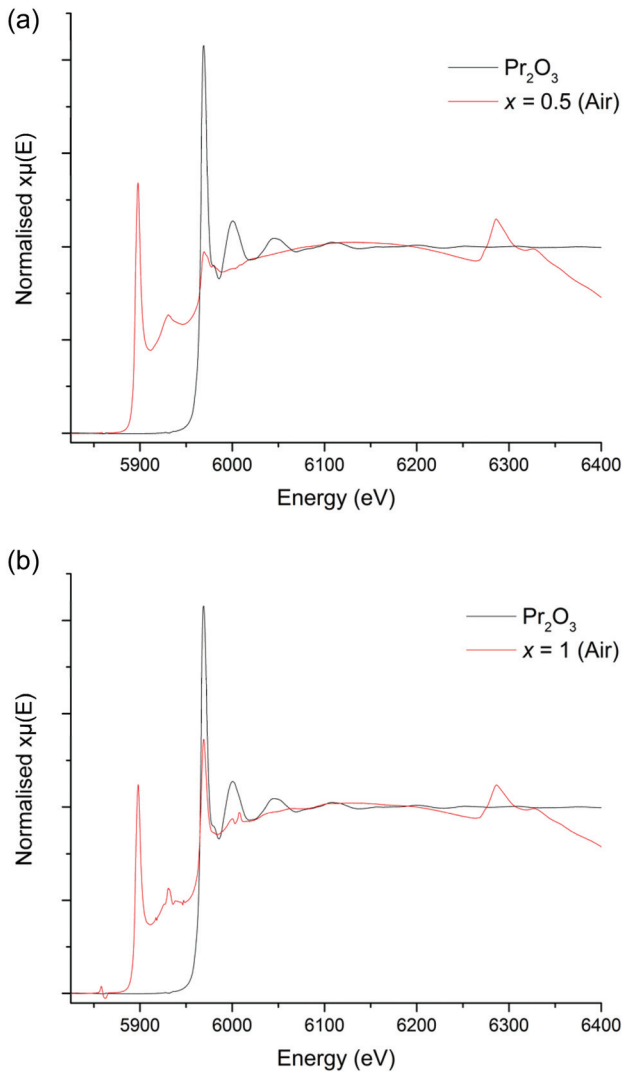

Fig. 7 (a) XANES spectra for $Li_5La_{2.5}Pr_{0.5}Nb_2O_{12}$ (air synthesised) compared to the Pr_2O_3 (Pr^{3+}) reference. (b) XANES spectra for $Li_5La_2Pr_1Nb_2O_{12}$ (air synthesised) compared to the Pr_2O_3 (Pr^{3+}) reference.

were similar to the results for equivalent $Li_5La_{3-x}Pr_xNb_2O_{12}$ phases synthesised under 5%H_2 (discussed below). The presence of the Li_3NbO_4 impurity in the air synthesised samples may suggest Nb site vacancies in the LLNO structure which have been filled by Pr^{4+}, which could account for the yellow powder colour. It could also be the case the Pr^{4+} is located on the La site. Therefore, these data suggest that there may be some partitioning of the Pr over both sites however, more work is needed to confirm whether this is so and to what extent.

In order to confirm the oxidation state of Pr in these samples, XANES data were collected on both x = 0.5 and 1, however, as outlined previously, in all cases the La L2 edge interfered somewhat with the Pr L3 edge. Nevertheless, the

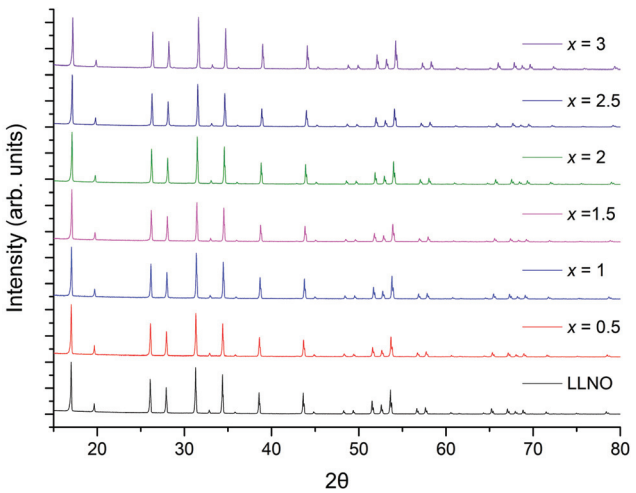

Fig. 8 The powder XRD patterns of $Li_5La_{3-x}Pr_xNb_2O_{12}$ ($0 \leq x \leq 3$) prepared in a reducing atmosphere (5%H_2). Phase pure samples with garnet type symmetry were obtained for all. For the small Li_3NbO_3 impurity see ESI† for expanded XRD pattern.

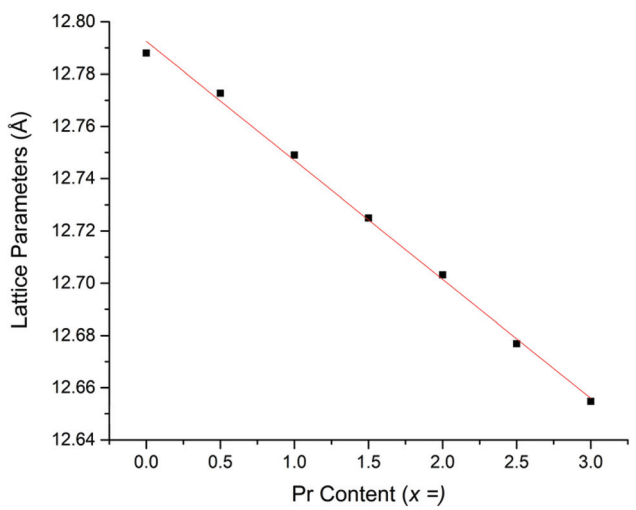

Fig. 9 Cell parameters *vs.* Pr content for 5%H_2 based synthesis of $Li_5La_{3-x}Pr_xNb_2O_{12}$.

Open Access Article. Published on 29 May 2020. Downloaded on 8/1/2025 2:51:58 AM.
This article is licensed under a Creative Commons Attribution-NonCommercial 3.0 Unported Licence.

XANES spectra of the $Li_5La_{2.5}Pr_{0.5}Nb_2O_{12}$ phase, which was prepared in air, does demonstrate characteristics of the Pr^{4+} reference (which would be consistent with presence of Pr^{4+} on either the Nb or La site), such as the peak broadness and the shoulder noted at 5982 eV, however the main peak appears to be positioned in line with the Pr_2O_3 reference at 5969 eV, consistent with mainly La site substitution, see Fig. 7a. However, the XANES spectra of the higher Pr content phase, $Li_5La_2Pr_1Nb_2O_{12}$, possesses only an absorption peak which is consistent with the Pr^{3+} reference at 5970 eV, Fig. 7b. Therefore, these spectra are somewhat contradictory but indicate, potentially, the presence of Pr in different oxidation states for $x = 0.5$, but not when $x = 1$ where only Pr^{3+} is seen.

The colours of the 5%H_2 synthesised garnets were increasingly vibrant green as the Pr content was increased, which indicates the presence of Pr^{3+}. Cell parameters determined from Rietveld refinement show a linear decrease with increasing Pr content, consistent with the smaller ionic radius of Pr^{3+} compared to La^{3+}, see Fig. 9. Despite the interference from the La L2 edge, the XANES data for these garnets are somewhat clearer than those derived from the $Li_{5+x}La_3Nb_{2-x}Pr_xO_{12}$ phases (Fig. 10a and b). The 5%H_2 prepared samples show a clear correlation with the Pr^{3+} reference (Pr_2O_3) in terms of peak intensity and characteristics, in both $x = 0.5$ and 1. Each phase has a strong absorption peak noted at 5970 eV, characteristic of Pr^{3+}, which matches both the Pr_2O_3 reference and other Pr^{3+} references used elsewhere.[52] When the Pr content is increased to $x = 1$, only increased absorbance occurs, as expected, but the peak characteristics remain unchanged. Hence, the characterisation data support the conclusion that only Pr^{3+} is present, and the different characteristics of the $x = 0.5$ phase prepared in air are unique to the synthesis method, as seen in the XANES data.

The XANES and XRD data for the H_2 synthesised samples therefore support the conclusion that Pr^{3+} has successfully been doped into the LLNO structure at the La site (24c).

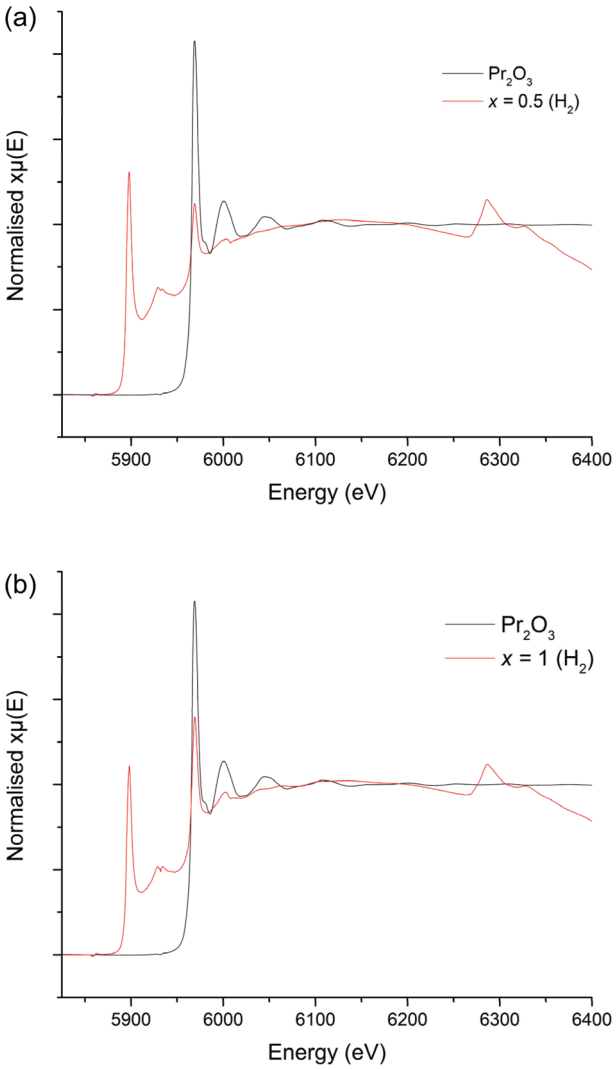

Fig. 10 (a) XANES spectra for $Li_5La_{2.5}Pr_{0.5}Nb_2O_{12}$ (5%H_2) compared to the Pr_2O_3 (Pr^{3+}) reference. (b) XANES spectrum for $Li_5La_2Pr_1Nb_2O_{12}$ (5% H_2) compared to the Pr_2O_3 (Pr^{3+}) reference.

SEM and EDX

SEM/EDX data for $Li_5La_{3-x}Pr_xNb_2O_{12}$ garnets, synthesised in air or H_2, showed uniform elemental distribution throughout the analysed grains, and have similar grain characteristics, see Fig. 11 and 12 respectively. The data for both air and H_2 synthesised samples demonstrated Pr and La present in the expected ratio. Hence EDX data supports the stoichiometric incorporation. However, the air synthesised samples did show some aluminium contamination, see Fig. 11, attributed to a reaction with the Al_2O_3 crucible.

Conductivity data for Nb site substitution: $Li_{5+x}La_3Nb_{2-x}Pr_xO_{12}$

Lithium ion conductivity was evaluated *via* impedance spectroscopy (a typical Nyquist impedance plot is shown in Fig. 13). A single non ideal semicircle was observed. A resistor, R1, in parallel with a constant phase element, CPE1, were used to fit the semicircle, and an inductor, L1, in series with R1/CPE1 was used to account for the inductance effect due to the limitations of the HP impedance spectroscopy equipment.

A characteristic spike relative to the semi-circle is present in all plots. This is attributed to a sample – electrode double layer effect. This spike represents the Li-ion transfer resistance between the garnet electrolyte and the Au electrode and corresponds to the capacitive behaviour of the gold electrodes which block Li-ion diffusion. As the semi-circle and tail were obtained in high and low frequency regions respectively it can be considered that conduction is primarily ionic in nature.[31]

The ionic conductivity of the $Li_{5+x}La_3Nb_{2-x}Pr_xO_{12}$ samples increased in line with increased Pr and hence lithium content (Fig. 14). The highest ionic conductivity of 5.6×10^{-4} S cm^{-1} at 50 °C was observed for $x = 0.8$, with a measured conductivity of 4.1×10^{-4} S cm^{-1} at 21 °C. See Table 1 and Fig. 14. These

This journal is © The Royal Society of Chemistry 2020

Open Access Article. Published on 29 May 2020. Downloaded on 8/1/2025 2:51:58 AM.
This article is licensed under a Creative Commons Attribution-NonCommercial 3.0 Unported Licence.

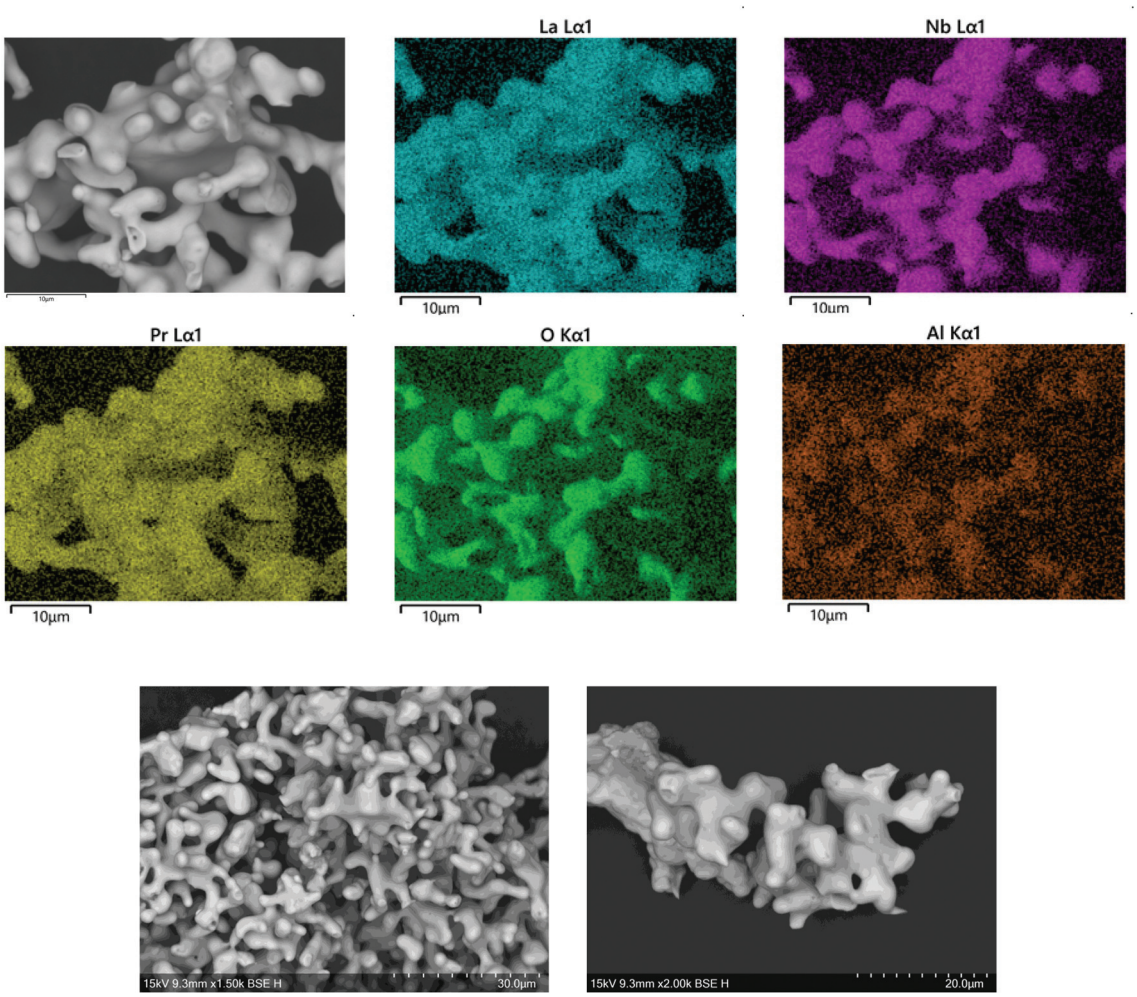

Fig. 11 SEM images and EDX map of elemental distribution in $Li_5La_2Pr_1Nb_2O_{12}$ (air). The presence of Al in this air synthesised sample is attributed to partial substitution onto the Li site. Al incorporation is often apparent in higher lithium content systems, and so this may support the postulation that there is some Pr^{4+} partitioning onto the Nb^{5+} site in the air synthesised $Li_5La_{3-x}Pr_xNb_2O_{12}$ samples. The corresponding H_2 synthesised sample, where only La site substitution is believed to occur, showed no Al contamination.

conductivity values represent some of the highest ever reported for garnets with Li content <6 per formula unit.

Higher content Pr phases ($x > 0.75$) were, however, prone to degradation during the high temperature densification treatment under N_2, resulting in small Pr_2O_3, La_2O_3 and $PrNb_5O_{14}$ impurities. In particular the XRD patterns for the $x = 1$ sample after N_2 sintering showed a more severe phase degradation. This degradation most likely accounts for the low relative pellet density of this sample and the resultant lower conductivity associated with this phase, as well as the non-linear temperature dependence of the Arrhenius plot, see Table 1 and ESI.† Consequently, further studies of samples with higher Pr contents, $x > 1$, were not performed (see ESI† for comparative XRD patterns before and after sintering treatments).

The activation energies for all samples (Fig. 14) ranged between 0.24–0.38 eV, which are similar to reports for other garnets, see Table 1.[51,54]

Conductivity data for La site substitution: $Li_5La_{3-x}Pr_xNb_2O_{12}$

All samples where Pr was doped on the La site showed similar conductivities to LLNO consistent with no change in Li content for this series. A typical Nyquist plot is displayed in Fig. 15a and b for air-based and H_2 synthesis respectively. These plots were fitted to two R/CPE components, representative of overlapping bulk and grain boundary resistance.

It was noted earlier that in the air synthesis samples, there may be some small level of Pr^{4+} substitution on the Nb site, which would be expected to give a small increase in Li content and hence conductivity. This was not observed, however these pellets proved difficult to densify, hence present with much lower relative densities than the corresponding undoped LLNO pellet. The influence of the poorer sintering may therefore mask any increase in conductivity from any Nb site substitution. Activation energies are similar to other reported garnets, see Table 2 and Fig. 16.[51,54]

Open Access Article. Published on 29 May 2020. Downloaded on 8/1/2025 2:51:58 AM.
This article is licensed under a Creative Commons Attribution-NonCommercial 3.0 Unported Licence.

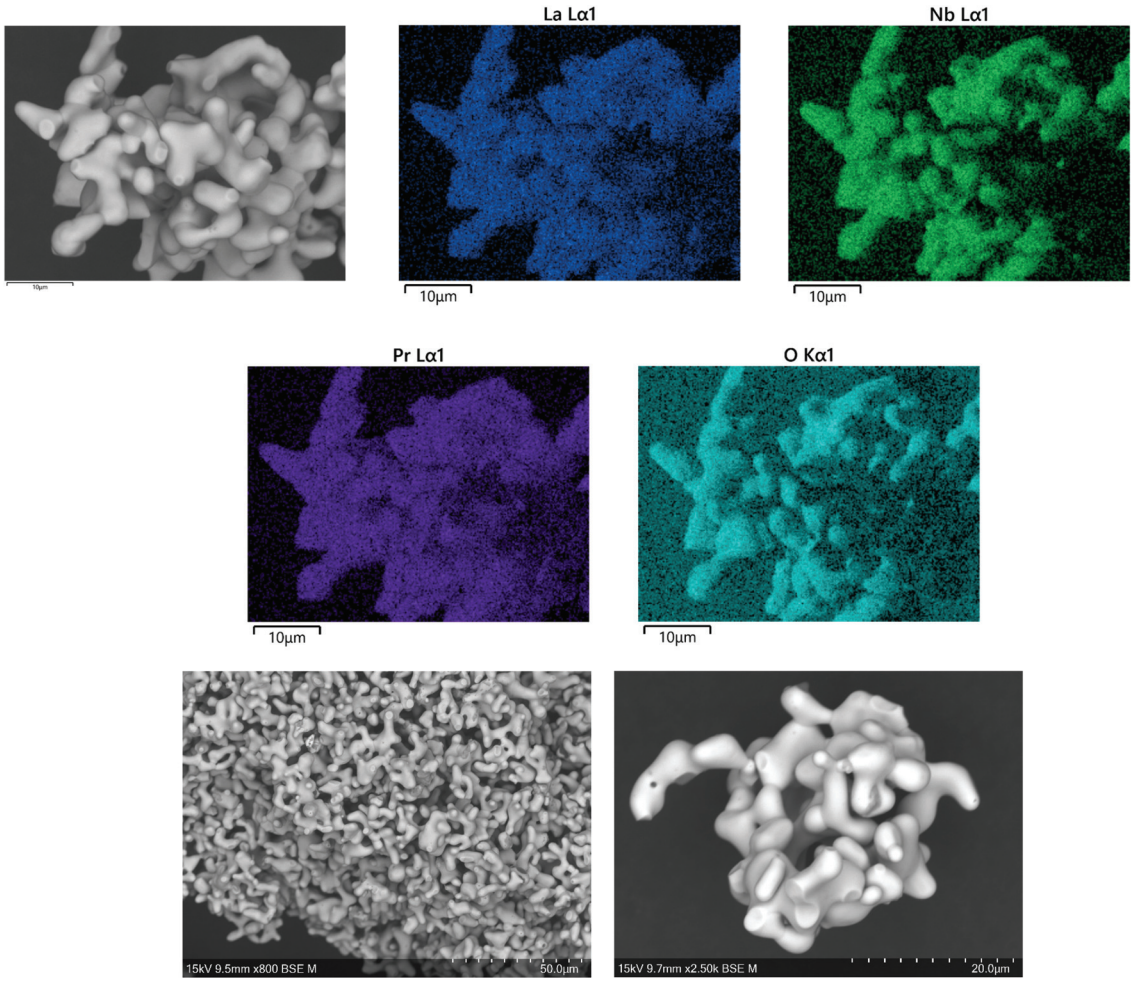

Fig. 12 SEM images and EDX map of elemental distribution in $Li_5La_{1.5}Pr_{1.5}Nb_2O_{12}$ (H_2). Since there is no increased Li content for Pr^{3+} doping on the La^{3+} site, therefore there is a decreased chance of Al exchange, hence no contamination from the alumina crucible is present.

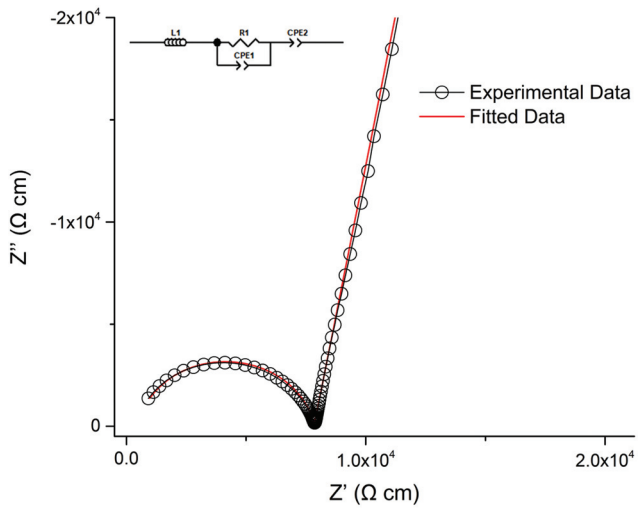

Fig. 13 Nyquist impedance plot for $Li_{5.75}La_3Nb_{1.25}Pr_{0.75}O_{12}$ at 30 °C which was fit the equivalent circuit in the top left.

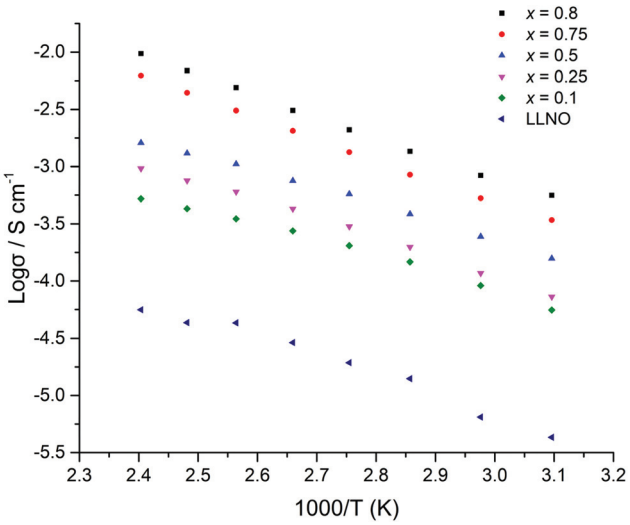

Fig. 14 Arrhenius plots for $Li_{5+x}La_3Nb_{2-x}Pr_xO_{12}$ (x = 0.1–0.8) samples which were hot pressed prior to sintering under N_2.

This journal is © The Royal Society of Chemistry 2020

Open Access Article. Published on 29 May 2020. Downloaded on 8/1/2025 2:51:58 AM.
This article is licensed under a Creative Commons Attribution-NonCommercial 3.0 Unported Licence.

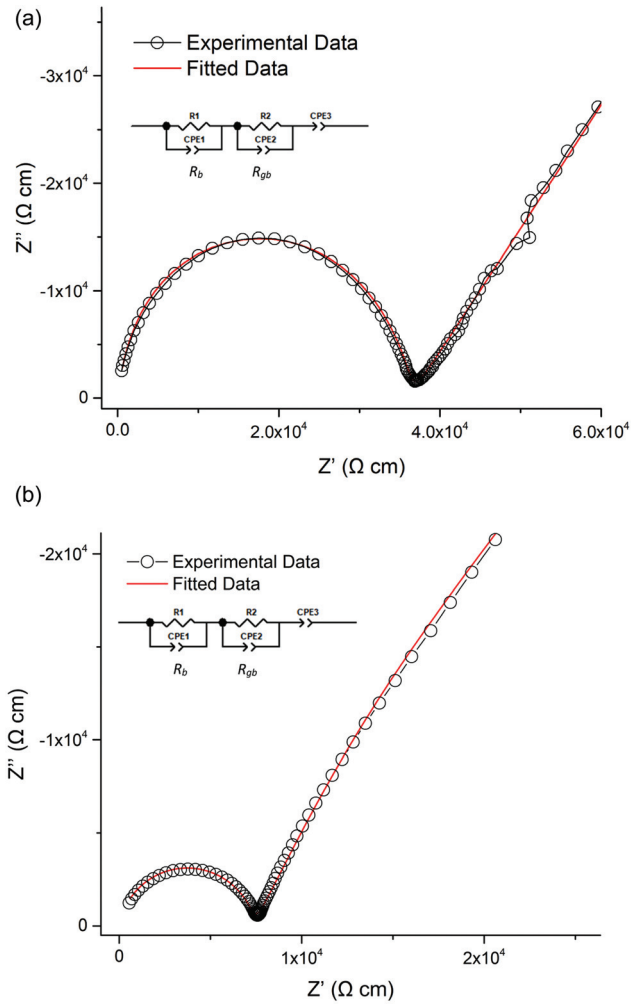

Fig. 15 (a) Nyquist impedance plot for $Li_5La_{3-x}Pr_xNb_2O_{12}$ at 130 °C for air-based synthesis. The fitted equivalent circuit is in the top left. R_b and R_{gb} relate to bulk and grain boundary resistivity respectively. (b) Nyquist impedance plot for $Li_5La_{3-x}Pr_xNb_2O_{12}$ at 130 °C for H_2 synthesis. The fitted equivalent circuit is in the top left. R_b and R_{gb} relate to bulk and grain boundary resistivity respectively.

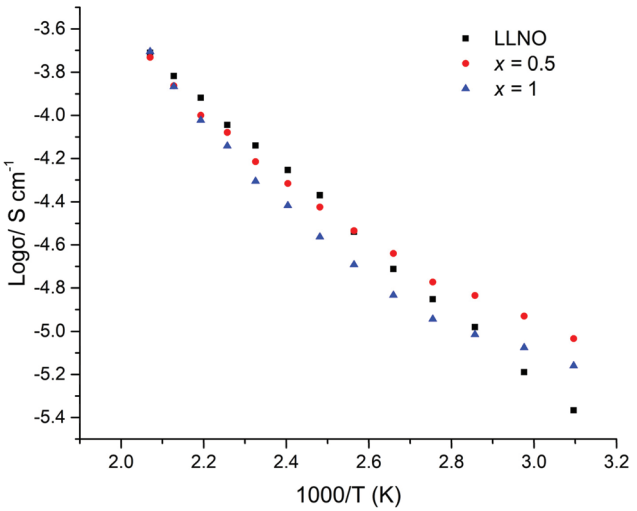

Fig. 16 Arrhenius plots for $Li_5La_{3-x}Pr_xNb_2O_{12}$ samples in air (x = 0–1).

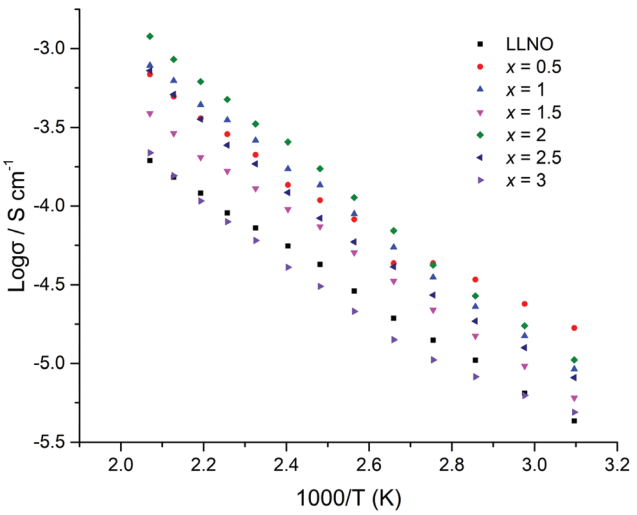

Fig. 17 Arrhenius plots for $Li_5La_{3-x}Pr_xNb_2O_{12}$ samples under H_2 (x = 0–3). The deviation from linearity at lower temperature for the x = 0.5 sample is attributed to partial water incorporation and subsequent loss on heating.

The H_2 synthesised samples showed similar conductivities for all samples, with a small peak in the conductivity of the series (1.7×10^{-5} S cm^{-1} (50 °C)) for x = 0.5, see Fig. 17 for Arrhenius plots. Activation energies fall within the 0.3–0.4 eV range, hence are similar to reports for other garnets, see Table 3.[51,54]

Samples with Pr doping at the La site showed far lower densities than the samples with Pr doping on the Nb site (see Tables 1–3). Hence Pr doping on the Nb site appears to also enhance the sintering compared to Pr doping on the La site, which may be related to the higher lithium content in these $Li_{5+x}La_3Nb_{2-x}Pr_xO_{12}$ systems.

Table 2 Pellet and conductivity data in addition to lattice parameters for $Li_5La_{3-x}Pr_xNb_2O_{12}$ samples synthesised in air

Sample	Pellet density (g cm^{-1})	Refined density (g cm^{-1})	Relative density (%)	Lattice parameters (Å)	Conductivity at 50 °C (S cm^{-1})	Activation energy 50–210 °C (eV)
LLNO	4.52	5.248	86	12.7880(3)	4.3×10^{-6}	0.32
x = 0.5	3.08	5.289	58	12.7701(3)	9.3×10^{-6}	0.25
x = 1	3.21	5.317	60	12.7481(3)	6.9×10^{-6}	0.28

Open Access Article. Published on 29 May 2020. Downloaded on 8/1/2025 2:51:58 AM.
This article is licensed under a Creative Commons Attribution-NonCommercial 3.0 Unported Licence.

Table 3 Pellet and conductivity data in addition to lattice parameters for $Li_5La_{3-x}Pr_xNb_2O_{12}$ samples synthesised under H_2

Sample	Pellet density (g cm^{-1})	Refined density (g cm^{-1})	Relative density (%)	Lattice parameters (Å)	Conductivity at 50 °C (S cm^{-1})	Activation energy 50–210 °C (eV)
LLNO reference[39]		5.259	—	12.79432	$\sim \times 10^{-6}$	
LLNO synthesized	4.52	5.248	86	12.7880(3)	4.3×10^{-6}	0.32
$x = 0.5$	3.87	5.286	73	12.7727(3)	1.7×10^{-5}	0.31
$x = 1$	3.40	5.316	64	12.7490(2)	9.2×10^{-6}	0.38
$x = 1.5$	3.47	5.346	65	12.7250(5)	6.0×10^{-6}	0.35
$x = 2$	3.91	5.373	73	12.7032(3)	1.1×10^{-5}	0.40
$x = 2.5$	3.72	5.407	69	12.6769(3)	8.1×10^{-6}	0.38
$x = 3$	4.01	5.435	74	12.6548(5)	4.9×10^{-6}	0.32

Conclusions

In summary, we have shown for the first time a dopant (Pr) that can be substituted onto both the La and Nb site in $Li_5La_3Nb_2O_{12}$. Furthermore, the oxidation state of the Pr is dictated by the site substitution; +3 on the La site, and +4 on the Nb site. Due to the resultant increase in Li content for Nb site substitution, a significant increase in conductivity is observed. These $Li_{5+x}La_3Nb_{2-x}Pr_xO_{12}$ samples show some of the highest conductivities for garnets with Li contents less than 6, with values up to 0.56 mS cm^{-1} (at 50 °C) for $x = 0.8$. A final point of note, Pr doped phases at the Nb site ($x \leq 0.25$) were a vibrant yellow, with a vibrant green colour obtained from H_2 based synthesis of $Li_{5+x}La_3Nb_{2-x}Pr_xO_{12}$ garnets when $x \geq 2.5$. Hence the optical properties of these garnets may merit further investigation, especially with respect to potential interest as pigments (see ESI†), however the effect of moisture on the Pr oxidation states, and therefore the sample colour, requires further investigation. It may also be of interest to study the optical properties of these Pr garnets under U.V. light.

Conflicts of interest

There are no conflicts of interest to declare.

Acknowledgements

We would like to thank the University of Birmingham for the studentship funding of Mark Stockham and the EPSRC for funding the GENESIS project (under EP/R024006/1). We thank the Diamond Light Source for the award of beam time as part of the Energy Materials Block Allocation Group SP14239. We would also like to thank Prof. Emma Kendrick for the continued use of the dry room facilities. Raw experimental data can be found at: https://doi.org/10.25500/edata.bham.00000490.

References

1 C.-X. Zu and H. Li, *Energy Environ. Sci.*, 2011, **4**, 2614–2624.
2 Y. Zhu, X. He and Y. Mo, *ACS Appl. Mater. Interfaces*, 2015, **7**, 23685–23693.
3 V. A. Agubra and J. W. Fergus, *J. Power Sources*, 2014, **268**, 153–162.
4 M. Armand and J. M. Tarascon, *Nature*, 2008, **451**, 652.
5 N. Nitta, F. Wu, J. T. Lee and G. Yushin, *Mater. Today*, 2015, **18**, 252–264.
6 M. Winter and R. J. Brodd, *Chem. Rev.*, 2004, **104**, 4245–4270.
7 J. M. Tarascon and M. Armand, *Nature*, 2001, **414**, 359.
8 J. Li, C. Ma, M. Chi, C. Liang and N. J. Dudney, *Adv. Energy Mater.*, 2015, **5**, 1401408.
9 Q. Liu, Z. Geng, C. Han, Y. Fu, S. Li, Y.-B. He, F. Kang and B. Li, *J. Power Sources*, 2018, **389**, 120–134.
10 A. C. Luntz, J. Voss and K. Reuter, *J. Phys. Chem. Lett.*, 2015, **6**, 4599–4604.
11 K. Fu, Y. Gong, B. Liu, Y. Zhu, S. Xu, Y. Yao, W. Luo, C. Wang, S. Lacey, J. Dai, Y. Chen, Y. Mo, E. Wachsman and L. Hu, *Sci. Adv.*, 2017, **3**, e1601659.
12 Y. Kato, S. Hori, T. Saito, K. Suzuki, M. Hirayama, A. Mitsui, M. Yonemura, H. Iba and R. Kanno, *Nat. Energy*, 2016, **1**, 16030.
13 V. Thangadurai, S. Narayanan and D. Pinzaru, *Chem. Soc. Rev.*, 2014, **43**, 4714–4727.
14 W. D. Richards, L. J. Miara, Y. Wang, J. C. Kim and G. Ceder, *Chem. Mater.*, 2016, **28**, 266–273.
15 B. Dong, R. Jarkaneh, S. Hull, N. Reeves-McLaren, J. J. Biendicho and A. R. West, *J. Mater. Chem. A*, 2016, **4**, 1408–1413.
16 C. Bernuy-Lopez, W. Manalastas, J. M. Lopez del Amo, A. Aguadero, F. Aguesse and J. A. Kilner, *Chem. Mater.*, 2014, **26**, 3610–3617.
17 H. Buschmann, J. Dölle, S. Berendts, A. Kuhn, P. Bottke, M. Wilkening, P. Heitjans, A. Senyshyn, H. Ehrenberg, A. Lotnyk, V. Duppel, L. Kienle and J. Janek, *Phys. Chem. Chem. Phys.*, 2011, **13**, 19378–19392.
18 S. Ohta, T. Kobayashi and T. Asaoka, *J. Power Sources*, 2011, **196**, 3342–3345.
19 T. Thompson, S. Yu, L. Williams, R. D. Schmidt, R. Garcia-Mendez, J. Wolfenstine, J. L. Allen, E. Kioupakis, D. J. Siegel and J. Sakamoto, *ACS Energy Lett.*, 2017, **2**, 462–468.
20 A. F. Wells, *Structural inorganic chemistry*, Clarendon Press, 1984.
21 E. J. Cussen and T. W. S. Yip, *J. Solid State Chem.*, 2007, **180**, 1832–1839.

 This journal is © The Royal Society of Chemistry 2020

Open Access Article. Published on 29 May 2020. Downloaded on 8/1/2025 2:51:58 AM.
This article is licensed under a Creative Commons Attribution-NonCommercial 3.0 Unported Licence.

22 D. Mazza, *Mater. Lett.*, 1988, **7**, 205–207.
23 J. Han, J. Zhu, Y. Li, X. Yu, S. Wang, G. Wu, H. Xie, S. C. Vogel, F. Izumi, K. Momma, Y. Kawamura, Y. Huang, J. B. Goodenough and Y. Zhao, *Chem. Commun.*, 2012, **48**, 9840–9842.
24 B. Dong, S. R. Yeandel, P. Goddard and P. R. Slater, *Chem. Mater.*, 2020, **32**, 215–223.
25 C. A. Geiger, E. Alekseev, B. Lazic, M. Fisch, T. Armbruster, R. Langner, M. Fechtelkord, N. Kim, T. Pettke and W. Weppner, *Inorg. Chem.*, 2011, **50**, 1089–1097.
26 M. A. Howard, O. Clemens, E. Kendrick, K. S. Knight, D. C. Apperley, P. A. Anderson and P. R. Slater, *Dalton Trans.*, 2012, **41**, 12048–12053.
27 S. Mukhopadhyay, T. Thompson, J. Sakamoto, A. Huq, J. Wolfenstine, J. L. Allen, N. Bernstein, D. A. Stewart and M. D. Johannes, *Chem. Mater.*, 2015, **27**, 3658–3665.
28 J. L. Allen, J. Wolfenstine, E. Rangasamy and J. Sakamoto, *J. Power Sources*, 2012, **206**, 315–319.
29 S.-W. Baek, J.-M. Lee, T. Y. Kim, M.-S. Song and Y. Park, *J. Power Sources*, 2014, **249**, 197–206.
30 M. Botros, R. Djenadic, O. Clemens, M. Möller and H. Hahn, *J. Power Sources*, 2016, **309**, 108–115.
31 R. Murugan, V. Thangadurai and W. Weppner, *Angew. Chem., Int. Ed.*, 2007, **46**, 7778–7781.
32 R. H. Brugge, J. A. Kilner and A. Aguadero, *Solid State Ionics*, 2019, **337**, 154–160.
33 Y. Jin and P. J. McGinn, *J. Power Sources*, 2011, **196**, 8683–8687.
34 S. Kim, M. Hirayama, S. Taminato and R. Kanno, *Dalton Trans.*, 2013, **42**, 13112–13117.
35 C. Loho, R. Djenadic, M. Bruns, O. Clemens and H. Hahn, *J. Electrochem. Soc.*, 2017, **164**, A6131–A6139.
36 S. Lobe, C. Dellen, M. Finsterbusch, H. G. Gehrke, D. Sebold, C. L. Tsai, S. Uhlenbruck and O. Guillon, *J. Power Sources*, 2016, **307**, 684–689.
37 C.-W. Ahn, J.-J. Choi, J. Ryu, B.-D. Hahn, J.-W. Kim, W.-H. Yoon, J.-H. Choi and D.-S. Park, *J. Electrochem. Soc.*, 2015, **162**, A60–A63.
38 B. Dong, L. L. Driscoll, M. P. Stockham, E. Kendrick and P. R. Slater, *Solid State Ionics*, 2020, **350**, 115317.
39 E. J. Cussen, *Chem. Commun.*, 2006, 412–413, DOI: 10.1039/B514640B.
40 V. Thangadurai, H. Kaack and W. J. F. Weppner, *J. Am. Ceram. Soc.*, 2004, **86**, 437–440.
41 S. Narayanan, F. Ramezanipour and V. Thangadurai, *J. Phys. Chem. C*, 2012, **116**, 20154–20162.
42 R. H. Brugge, A. K. O. Hekselman, A. Cavallaro, F. M. Pesci, R. J. Chater, J. A. Kilner and A. Aguadero, *Chem. Mater.*, 2018, **30**, 3704–3713.
43 G. Larraz, A. Orera and M. L. Sanjuán, *J. Mater. Chem. A*, 2013, **1**, 11419–11428.
44 C. Galven, J. Dittmer, E. Suard, F. Le Berre and M.-P. Crosnier-Lopez, *Chem. Mater.*, 2012, **24**, 3335–3345.
45 B. Toby and R. Dreele, *J. Appl. Crystallogr.*, 2013, **46**, 544–549.
46 B. Ravel and M. Newville, *J. Synchrotron Radiat.*, 2005, **12**, 537–541.
47 J. Percival, D. Apperley and P. R. Slater, *Solid State Ion.*, 2008, **179**, 1693–1696.
48 J. A. Badenes, J. B. Vicent, M. Llusar, M. A. Tena and G. Monr, *J. Mater. Sci.*, 2002, **37**, 1413–1420.
49 G. Del Nero, G. Cappelletti, S. Ardizzone, P. Fermo and S. Gilardoni, *J. Eur. Ceram. Soc.*, 2004, **24**, 3603–3611.
50 M. Shoyama, H. Nasu and K. Kamiya, *Preparation of Rare Earth-Zircon Pigments by the Sol-Gel Method*, 1998.
51 S. Ramakumar, C. Deviannapoorani, L. Dhivya, L. S. Shankar and R. Murugan, *Prog. Mater. Sci.*, 2017, **88**, 325–411.
52 T. Ogier, C. Prestipino, S. Figueroa, F. Mauvy, J. Mougin, J. C. Grenier, A. Demourgues and J. M. Bassat, *Chem. Phys. Lett.*, 2019, **727**, 116–120.
53 R. C. Karnatak, J. M. Esteva, H. Dexpert, M. Gasgnier, P. E. Caro and L. Albert, *Phys. Rev. B: Condens. Matter Mater. Phys.*, 1987, **36**, 1745–1749.
54 J.-F. Wu, E.-Y. Chen, Y. Yu, L. Liu, Y. Wu, W. K. Pang, V. K. Peterson and X. Guo, *ACS Appl. Mater. Interfaces*, 2017, **9**, 1542–1552.